

Double-leaf Riemann surface topological converse magnetoelectricity

Ying Zhou,^{1,*} Haoshen Ye,^{1,*} Junting Zhang,^{2,†} and Shuai Dong^{1,‡}

¹Key Laboratory of Quantum Materials and Devices of Ministry of Education,
School of Physics, Southeast University, Nanjing 211189, China

²School of Materials Science and Physics, China University of Mining and Technology, Xuzhou 221116, China

Electric field control of magnetism in solids, i.e. the converse magnetoelectricity, is highly desired for applications of scalable energy-efficient logic devices. However, it is not only a technical challenge but also a scientific paradox, since in principle the electric and magnetic degrees of freedom obey distinct rules of symmetries. Despite the great progresses obtained in the community of multiferroics during the past decades, the success of magnetoelectricity remains on its way and more alternative approaches with conceptual revolution are urgently needed. Here, by introducing the concept of topology into multiferroics, an exotic magnetoelectric double-leaf Riemann-surface is unveiled based on the mechanism of spin-dependent $d-p$ hybridization in a two-dimensional magnet: GdI₂ monolayer. Protected by the topology, a 180° spin reversal can be precisely achieved by an electric cycle, leading to a robust and dissipationless converse magnetoelectric function. Such a topological magnetoelectricity allows the nontrivial manipulation of magnetization by AC electric field. In this category, more candidate materials with better performance are designed targetedly, which pave the road to the potential applications with topological magnetoelectrics.

I. INTRODUCTION

Symmetry and topology are two important mathematical concepts, which often govern the physics in explicit or implicit manners. In condensed matter, ideal examples are ferroelectrics and ferromagnets, which break the spatial inversion and time reversal symmetries respectively. And the nontrivial topology can lead to the so-called topological protected physical properties, e.g., dissipationless edge transport in materials with topological electronic/photonic/phononic band structures in moment space [1–3]. The concept of topology has also been introduced to the magnetoelectric research. The most intuition cases are some topological ferroic textures, such as vortices/skyrmions/merons of spin moments or electric dipoles [4–7]. These manifestations of topology in moment space and real space form different branches of topological entities in matter, as summarized in Fig. 1.

Expected by the demanding of next generation information devices, magnetoelectricity in solids, namely the electric field control of magnetism or magnetic control of electric polarity, is highly valued for applications [8–10]. However, limited by their distinct symmetries, the intrinsic magnetoelectricity are naturally difficult, while other ingredients must be involved as the intermediary to glue the spin polarity and electric polarity [8, 11]. Till now, it remains challenging to directly and efficiently reverse the magnetization via electrical field, a key magnetoelectric function. Some approaches have been proposed to overcome this difficulty. For example, a two-step 90° rotation of magnetization can lead to a net 180° reversal, via the piezoelectric tuning of magnetocrystalline

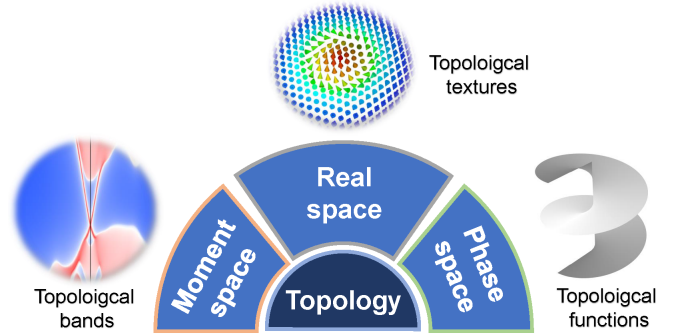


FIG. 1. Branches of topology in matter. There are topological band structures in moment space, topological textures of in real space, and topological functions in phase space. These branches are different in physical manifestations, but uniform in their mathematic root.

anisotropy [12]. The electrical tuning of charge disproportion in ferrimagnetic systems can also reverse the net magnetization [13, 14]. A recent theory also proposed that the dynamics of a Néel-type magnetic domain can resize the ferromagnetic domains during the reversal of chirality [15].

Very recently, another kind of topology, i.e. topological functions in magnetoelectric phase space (Fig. 1), was unveiled in several multiferroics with complex antiferromagnetic structures. In GdMn₂O₅, a topologically protected magnetoelectric switching coined as “magnetic crankshaft” was identified, which can convert the increasing-and-decreasing cycle of magnetic field into a circular spin rotation [16]. While in TbMn₃Cr₄O₁₂, the magnetism induced ferroelectric polarization can span a Roman surface, a three-dimensional non-oriented topological object, which can be traced via an ergodic rotation of spin orientation [17, 18]. These intrinsic topologies lead to exotic magnetoelectric functions under magnetic

* These authors contributed equally to this work

† juntinzhang@cumt.edu.cn

‡ sdong@seu.edu.cn

field, which lead to conceptual revolution of magnetoelectricity and extend the territory of topology in condensed matter.

Here we propose another kind of topological magnetoelectric function in phase space, coined as the double-leaf Riemann surface converse magnetoelectricity, which should generally exist in various non-centrosymmetric magnets. For simplicity and practicality, we use the ferromagnetic GdI₂ monolayer as the first model system, since its corresponding van der Waals (vdW) bulk is experimentally existing [19]. In the following, we will demonstrate how the double-leaf Riemann surface topology provides a robust solution to the long-term challenge of electric field reversal of magnetization. And the general conditions will also be clarified and more candidate materials in this category will also be suggested.

II. MODEL & METHODS

A. First-principles calculations

The first-principles calculations based on density functional theory (DFT) were performed using the projector-augmented wave (PAW) method, as implemented in the Vienna *ab initio* Simulation Package (VASP) [20–22]. The Perdew-Burke-Ernzerhof functional was used as the exchange-correlation functional [23, 24]. A vacuum space of 20 Å was added to avoid interaction between neighboring periodic images. We used a cutoff energy of 600 eV for the plane-wave bases, and a Γ -centered $15 \times 15 \times 1$ k -point mesh for the Brillouin zone integration. The in-plane lattice constants and internal atomic coordinates were relaxed until the Hellman-Feynman force on each atom is less than 0.005 eV/Å. A convergence threshold of 10^{-7} eV was used for the electronic self-consistency loop. To describe correlated $4f$ electrons of Gd, the GGA+ U method is applied [25], and the adopted U_{eff} is 8 eV for Gd's $4f$ orbitals [26]. For comparison, Heyd-Scuseria-Ernzerhof (HSE06) hybrid functional was also considered [27].

Phonon band structures were calculated using density functional perturbation theory (DFPT). The phonon frequencies and corresponding eigen-modes were calculated on the basis of the extracted force-constant matrices with a $4 \times 4 \times 1$ supercell, as implemented in the PHONOPY code [28]. The ferroelectric polarization was calculated by using the Berry phase method [29]. The unit volume of ferroelectric polarization is measured by atomic layer thickness (removing the thickness of the vacuum layer). In addition, Monte Carlo simulations were performed to verify the magnetic ground states and estimate the magnetic transition temperatures.

B. Landu-Lifshitz-Gilbert

The simulation is based on the classical spin model, which can be written as:

$$H = -J_{ij} \sum_{\langle i,j \rangle} \mathbf{S}_i \cdot \mathbf{S}_j - A \sum_i (\mathbf{S}_i^z)^2, \quad (1)$$

with J and A as the exchange parameters and the anisotropy constant. The nearest neighboring J_1 , next-nearest neighboring J_2 , and third-nearest neighboring J_3 are considered, which can be extracted from DFT energies.

In micromagnetic simulation, the spin dynamics are described by the Landu-Lifshitz-Gilbert (LLG) equation:

$$\frac{\partial \mathbf{S}_i}{\partial t} = -\frac{\gamma}{(1 + \alpha^2)} \mathbf{S}_i \times (\mathbf{H}_{\text{eff}}^i + \alpha \mathbf{S}_i \times \mathbf{H}_{\text{eff}}^i), \quad (2)$$

where $\alpha = 0.01$ is the Gilbert damping constant, γ is the Gilbert gyromagnetic ratio, and $\mathbf{H}_{\text{eff}}^i = -\frac{1}{M} \frac{\partial H}{\partial \mathbf{S}_i}$ is the effective field derived from the Hamiltonian H (Eq. 1 plus the electrostatic energy $-\sum_i \mathbf{E} \cdot \mathbf{P}_i$), where M is the magnetic moment of Gd.

The LLG equation is solved by the fourth order Runge-Kutta method with time steps $dt \ll T = \frac{1}{f}$. The sinusoidal AC electric field is described as $\mathbf{E}(t) = \mathbf{E}_0 \sin(2\pi ft)$. The pulse sequence used in the four electrode configuration is consisted by alternate half-periodic sinusoidal waves.

III. RESULTS AND DISCUSSION

A. Static magnetoelectricity in GdI₂

The structure of GdI₂ monolayer is non-centrosymmetric and nonpolar (space group $P\bar{6}m2$, No. 187), as shown in Fig. 2(a), although its corresponding vdW bulk is centrosymmetric due to its 2H-MoS₂-type AB stacking mode [19, 26]. Wang *et al.* proved its possibility of exfoliation [26], with a low cleavage energy 0.26 J/m², lower than the experimental value of graphite (0.36 J/m²). As shown in Fig. 1(b), the Gd²⁺ ion locates at the center of trigonal prism, and there are eight unpaired electrons, forming the $4f^7 5d^1$ orbital configuration, as confirmed by our density functional theory (DFT) calculation and previous study [26]. According to the crystal field of distorted trigonal prism, the residual $5d$ electron stays at a singlet orbital, which is a hybrid one of the $3z^2 - r^2/x^2 - y^2/xy$ orbitals [30], as visualized in Fig. 2(b). The electronic band structure and orbital-projected density of states can be found in Fig. S1 in Supplementary Materials (SM) [31]. Such an orbital occupancy leads to an easy-plane magnetocrystalline anisotropy. Our DFT calculation finds the magnetocrystalline anisotropy energy (MAE) is ~ 0.7 meV/Gd, as shown in Fig. 1(c). The local

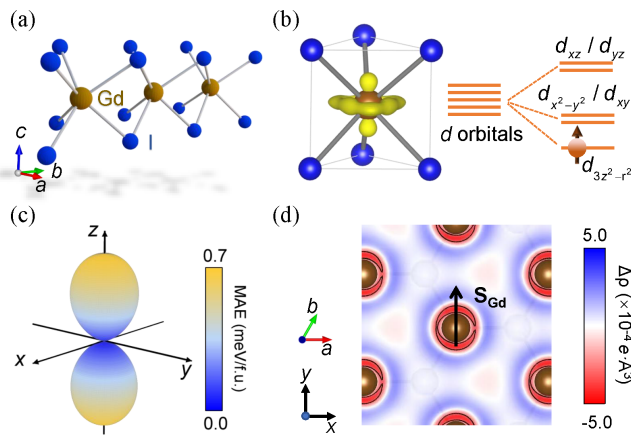


FIG. 2. Structure and magnetic properties of GdI₂ monolayer. (a) Crystal structure. (b) Schematic of the prism-type crystalline field splitting of GdI₂ monolayer. The orbital occupancy of $5d^1$ can be visualized by the electron cloud obtained in DFT calculation. (c) Plot of MAE. The z -axis is along the out-of-plane direction. (d) Differential electron density $\Delta\rho(r)$ for Gd's spin along the y -axis. Here $\Delta\rho(r)$ is defined as the difference of electron spatial distribution induced by SOC.

magnetic moment is $8 \mu_B/\text{Gd}$ and the magnetic ground state is ferromagnetic (Fig. S3 and Table S1 in SM [31]), as inherited from its vdW bulk with a near room-temperature Curie temperature ($T_C = 241$ K for monolayer and 313 K for bulk) [26, 32]. And the monolayer is an insulator with a band gap 0.6 eV/ 1.1 eV according to the DFT/ Heyd-Scuseria-Ernzerhof (HSE06) hybrid functional calculation (Fig. S2 in SM [31]), in consistent with the previous result [26].

Although its space group $P\bar{6}m2$ is nonpolar, the magnetic point group (MPG) can become polar, depending on the spin orientation. Then a finite ferroelectric polarization can be induced by magnetism, as a character of the type-II multiferroicity [11]. Microscopically, the spin-orbit coupling (SOC) plays a key role to generate the polarization. An intuitive result can be visualized in Fig. 2(d): when the spin of Gd²⁺ (\mathbf{S}_{Gd}) points along the y -axis, the contour map of electron density shows slight asymmetry at the Gd site along the x -axis, indicating the emergence of electronic polarization along the x -axis. The concrete physics is analyzed as follow.

With the ferromagnetic \mathbf{S}_{Gd} lying in the xy plane, the out-of-plane 3-fold rotation (C_3) symmetry is broken, which allows the in-plane polarization. For example, when \mathbf{S}_{Gd} is along the x -axis which is a 2-fold rotation axis, the MPG becomes $m'm'2$, whose polar axis is also along the x -axis. The MPG becomes $m'm2'$ once \mathbf{S}_{Gd} pointing along the y -axis, but its polar axis remains along the x -axis. For \mathbf{S}_{Gd} along other arbitrary in-plane directions, the MPG becomes m' , which allows both nonzero x - and y -components of polarization (i.e. P_x and P_y), as shown in Fig. 3(a) and Table S2 in SM [31].

Above symmetry analysis has given a phenomenological and qualitative description of magnetoelectricity, and

its microscopic quantum mechanism will be clarified as follow. Due to the ferromagnetic configuration, neither the inverse Dzyaloshinskii-Moriya interaction nor the exchange striction is responsible for the magnetism induced polarization. Then the possible route to type-II multiferroicity here is the so-called spin-dependent $p-d$ hybridization mechanism, which originates from the modification $p-d$ hybridization by SOC [33–35]. Analytically, the magnetism induced polarization can be obtained by summing the charge transfers between the magnetic ion and its six ligands [36]:

$$\mathbf{P} \propto \sum_{i \in [1-6]} (\mathbf{S}_{\text{Gd}} \cdot \mathbf{e}_i)^2 \cdot \mathbf{e}_i, \quad (3)$$

where \mathbf{e}_i is the unit vector of the bond between the magnetic ion and ligand. Once \mathbf{S}_{Gd} lies in the xy plane, it is straightforward to obtain the analytic expression:

$$\begin{aligned} \mathbf{P} &= (P_x, P_y, P_z) \\ &\propto (S_x^2 - S_y^2, -2S_x S_y, 0) \\ &= [\cos(2\varphi_S), -\sin(2\varphi_S), 0] \end{aligned} \quad (4)$$

where φ_S is the azimuthal angle of \mathbf{S}_{Gd} as defined in Fig. 3(a). The polar plots of P_x and P_y as a function of φ_S are shown as curves in Figs. 3(b) and 3(c), respectively.

Such analytic results are further confirmed by our DFT calculations [dots in Figs. 3(b-c)], implying that the spin-dependent $p-d$ hybridization is indeed the underlying mechanism. The magnitude of \mathbf{P} is a constant, reaching $125 \mu\text{C}/\text{m}^2$ (by using the thickness of GdI₂ monolayer to estimate the volume), which is comparable to other multiferroics in this category (e.g. $100 \mu\text{C}/\text{m}^2$ for Ba₂CoGe₂O₇ and $21.2 \mu\text{C}/\text{m}^2$ for Ca₃FeReO₇) [33, 34].

Considering the direct coupling between spin orientation (i.e. the magnetization \mathbf{M}) and polarization \mathbf{P} , it is natural to expect intrinsic magnetoelectricity, namely using the magnetic field \mathbf{H} to control \mathbf{P} (i.e. the direct magnetoelectric effect, DME), or using the electric field \mathbf{E} to control \mathbf{M} (i.e. CME). As shown in Fig. 3(d), by rotating the in-plane magnetic field \mathbf{H} quasi-statically for a cycle, the magnetization (i.e. \mathbf{S}_{Gd}) will rotate synchronously, but the induced polarization \mathbf{P} will rotate with a twice angular velocity. Conversely, as shown in Fig. 3(e), by rotating the in-plane electric field \mathbf{E} quasi-statically for a cycle, the polarization \mathbf{P} will rotate synchronously, but the associated \mathbf{S}_{Gd} will rotate with a half angular velocity. Thus, a cycle of quasi-static \mathbf{E} will reverse \mathbf{M} for 180° , which is a long-desired function of CME. Then two continuous cycles of quasi-static \mathbf{E} will restore \mathbf{M} to its original direction.

The magnetoelectricity of GdI₂ monolayers can be summarized in Fig. 3(f). The coupling between electric and magnetic degrees of freedom can be analogous to a gear set with 1:2 perimeters. Mathematically, such a magnetoelectric behavior obeys the topology of double-leaf Riemann surface. Only even winding number of \mathbf{E} can restore \mathbf{M} , while any odd winding number of \mathbf{E} can only

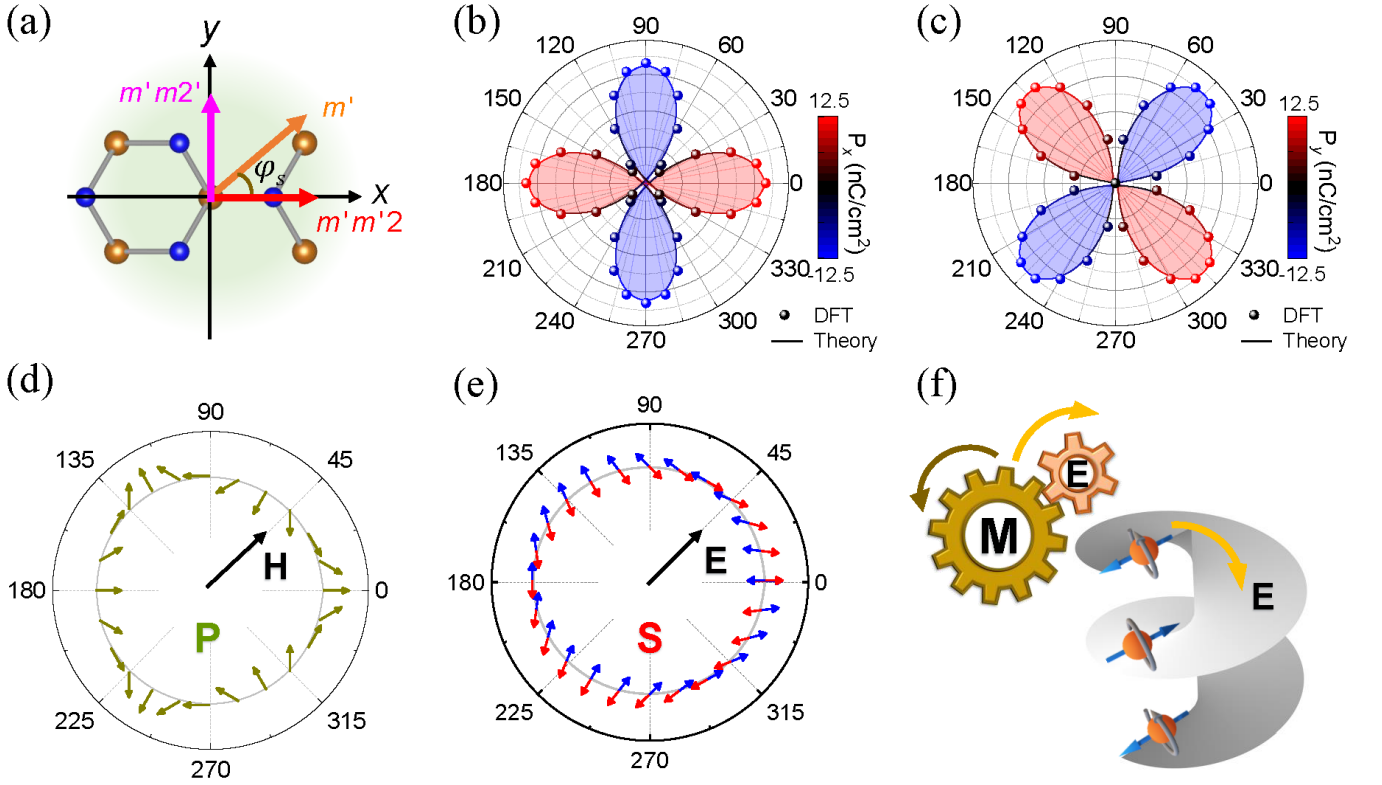


FIG. 3. Double-leaf Riemann surface magnetoelectricity in GdI_2 monolayer. (a) The evolution of MPG as a function of \mathbf{S}_{Gd} 's orientation (characterized by its azimuthal angle φ_S). Orange arrow: generic case of \mathbf{S}_{Gd} . Red/pink arrows: the special cases of \mathbf{S}_{Gd} along the x/y axes, which reserve partial symmetries. (b-c) In-plane components of magnetism induced polarization (P_x and P_y) as a function of azimuthal angle φ_S . Dots: numerical results obtained from DFT calculations; Curves: Analytic fitting from the theory of spin-dependent $d-p$ hybridization. (d) The evolution of polarization (green vector) upon the rotation of in-plane magnetic field \mathbf{H} . (e) The evolution of spin direction (i.e. the magnetization \mathbf{M}) upon the rotation of in-plane electric field \mathbf{E} . Red/blue arrows correspond to the odd/even cycle of rotating \mathbf{E} . (f) The one cycle rotation of \mathbf{E} leads to half cycle rotation of \mathbf{M} , mimicking a gear set with 1:2 perimeters. This magnetoelectric behavior forms the topologic double-leaf Riemann surface, which is a non-oriented surface with a half twist. Then protected by the topology, only even winding number of \mathbf{E} can restore \mathbf{M} , while any odd winding number of \mathbf{E} can only flip \mathbf{M} by 180° robustly and precisely.

flip \mathbf{M} by 180° , protected by the topology of double-leaf Riemann surface which originates from the mathematic formula of $(\mathbf{S} \cdot \mathbf{e})^2$. In addition, since both the $|\mathbf{P}|$ and MAE are isotropic in the xy plane, ideally such an in-plane rotation of quasi-static \mathbf{E} or \mathbf{H} does not need to overcome any energy barriers, and thus dissipationless.

B. Dynamic magnetoelectricity in GdI_2

Above topological double-leaf Riemann surface magnetoelectricity is straightforward based on the protocol of quasi-static electric/magnetic cycles. However, for information reading/writing in potential magnetoelectric logic devices, dynamic process must be involved. Here we employ the Landau-Lifshitz-Gilbert (LLG) equation to describe the dynamics of \mathbf{S}_{Gd} and associated polarization.

First, starting from the case with \mathbf{S}_{Gd} along the x -axis (i.e. \mathbf{P} also along the x -axis), the intrinsic switching du-

ration is estimated by applying a static electric field \mathbf{E} along the $-x$ direction. As shown in Figs. 4(a-b) and movie S1 in SM [31], under a moderate field 1 kV/cm , \mathbf{P} is reversed within 5 ns , accompanying by a 90° rotation of \mathbf{S}_{Gd} . This dynamic process is fast in the beginning and becomes slower in the home stretch. This switching duration (T_{90}) is in proportional to the $1/|\mathbf{E} \cdot \mathbf{P}|$, as expected from the LLG equation [Fig. 4(c) and Fig. S4 in SM [31]]. Thus, the larger \mathbf{E} (or \mathbf{P}), the faster magnetoelectric switching.

Second, once an AC electric field $\mathbf{E}(t)$ is applied along the x -axis, the dynamic behavior becomes frequency dependent, as shown in Fig. 4(d) and movie S2 in SM [31]. In the low-frequency region, e.g. $f = 50 \text{ MHz}$, the dynamics of spin and dipole can fully follow the AC $\mathbf{E}(t)$, forth and back periodically [Fig. 4(d) and Fig. S5(a) in SM [31]]. In the high frequency cases, e.g. $f = 500 \text{ MHz}$, \mathbf{S}_{Gd} and \mathbf{P} can not follow $\mathbf{E}(t)$ anymore, the flippings of spin and dipole are only partially and oscillating around the middle point: 90° (or 270°) for \mathbf{P} and 315° (or 45°)

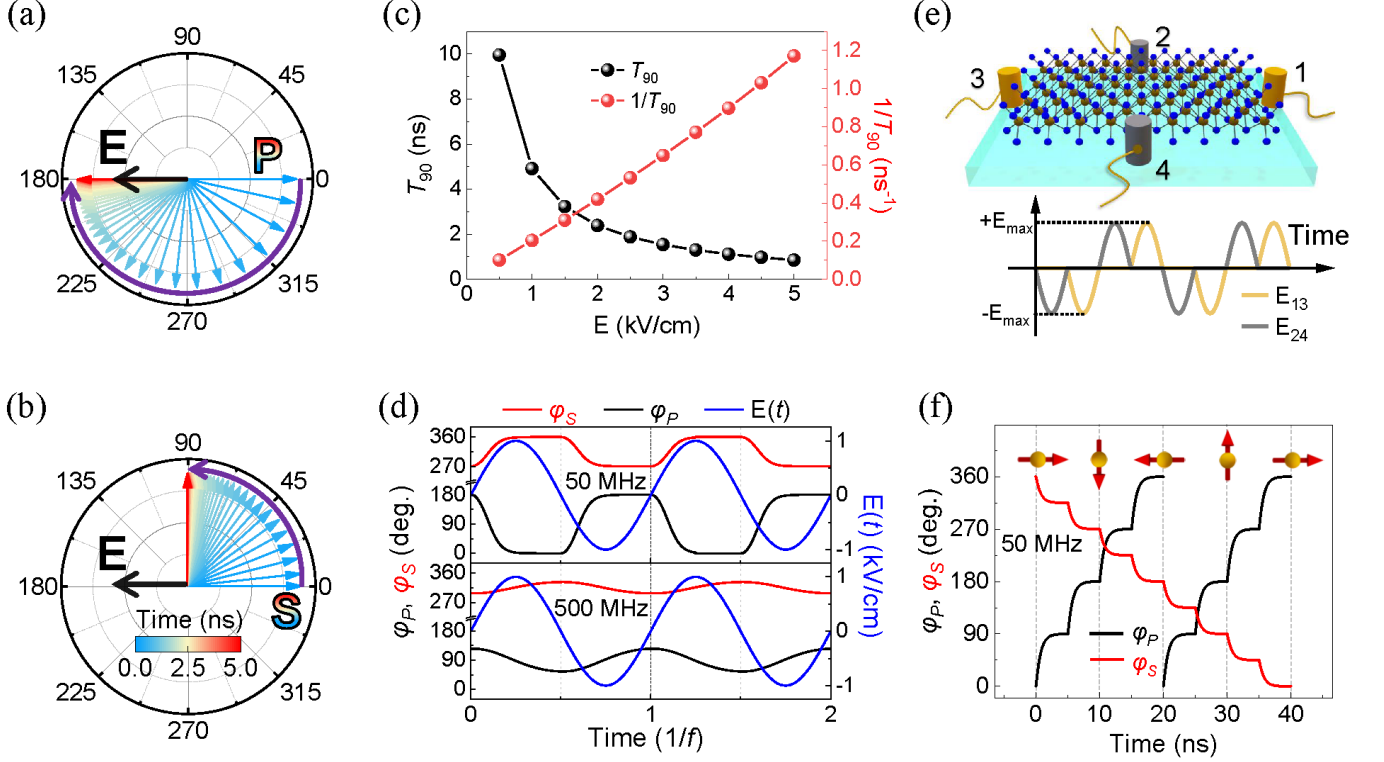


FIG. 4. Electrical response of \mathbf{P} and \mathbf{S}_{Gd} . The rotation dynamics of \mathbf{P} (a) and \mathbf{S}_{Gd} (b) excited by static electric field of 1 kV/cm. The black arrow denotes direction of electric field. (c) The evolution of switching duration T_{90} (and its reciprocal $1/T_{90}$) as a function of static electric field \mathbf{E} . (d) Oscillation of \mathbf{P} and \mathbf{S}_{Gd} excited by sinusoidal AC electric field $E(t)$ of $f = 50$ MHz (top) and $f = 500$ MHz (bottom). φ_S and φ_P are azimuthal angles of \mathbf{S}_{Gd} and the corresponding polarization \mathbf{P} . (e) Schematic diagram of four electrodes in perpendicular configuration. Inset: a period of alternate electric field pulses. (f) The half-harmonic dynamics of \mathbf{S}_{Gd} excited by pulse-width modulated electric field sets of $f = 50$ MHz. Inset: direction of \mathbf{S}_{Gd} . In all cases, initial \mathbf{P} and \mathbf{S}_{Gd} are oriented to the $+x$ direction, and the maximum of AC electric fields are 1 kV/cm.

for \mathbf{S}_{Gd} [Fig. 4(d) and Fig. S5(b) in SM [31]].

Third, to obtain the topological winding of \mathbf{P} and \mathbf{S}_{Gd} , four electrodes are arranged in the perpendicular configuration, as depicted in Fig. 4(e). Then a sequence of alternate electric field pulses (E_{13} & E_{24}) is applied, also shown in Fig. 4(e) and Fig. S6 in SM [31]. At low frequency, e.g. $f = 50$ MHz, each pulse can generate a 90° rotation of \mathbf{P} and 45° rotation of \mathbf{S}_{Gd} . Then eight pulses leads to a full winding cycle of \mathbf{S}_{Gd} and twice cycles of \mathbf{P} , as shown in Fig. 4(f) and movie S3 in SM [31].

Finally, it should be noted that the surrounding magnetic field generated by the AC electric field orientates to the out-of-plane direction. Its Zeeman energy is in the order of $\sim 0.15 \mu\text{eV}/\text{Gd}$, which is negligible compared to its MAE ($0.7 \text{ meV}/\text{Gd}$). Thus, this double-leaf Riemann surface magnetoelectricity with in-plane rotations of \mathbf{S}_{Gd} and \mathbf{P} is electrically driven.

C. General rules & more candidates

Although above studies only focused on GdI_2 monolayer, the physical mechanism should generally apply to more systems. The spin-dependent p - d hybridization can

induce ferroelectricity only in those point groups lacking inversion symmetry. In the 2D case, there are eighteen noncentrosymmetric point groups. Their magnetoelectric tensors are derived, as summarized in Supplementary text. According to these tensors, half of them [class A in Fig. 5(a)] do not permit the in-plane polarization originated from spin-dependent p - d hybridization when the ferromagnetic spins lying in the ab -plane.

For those point groups in class B, although there is still a 1 : 2 relationship between the spin and polarization modulation period, the double-leaf Riemann converse magnetoelectricity is not guaranteed, since the trajectory of polarization may not pass through all four quadrants (e.g. Fig. S7(a) and Fig. S8(b) in SM [31]). Even if the trajectory of polarization can pass through all four quadrants (e.g. Fig. S7(b-c) and Fig. S8(a) in SM [31]), the amplitude of polarization is not a constant, but depends on its orientation. Further, the in-plane magnetocrystalline anisotropy will arise. These two factors establish energy barriers during the spin/dipole rotation, which lead to energy dissipation for converse magnetoelectricity.

Only those point groups in class C, which contain a common 3-fold rotational symmetry (C_3), allow the dis-

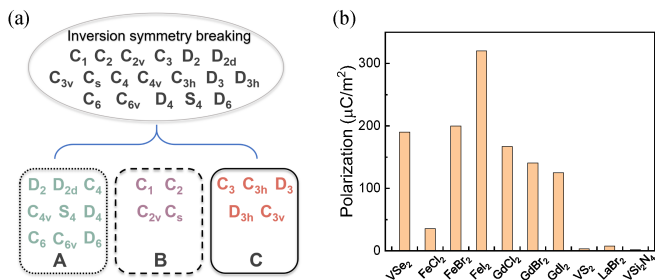


FIG. 5. Symmetry classification and more candidates. (a) Symmetry classification of 2D noncentrosymmetric point groups in terms of spin-induced polarization. The ferromagnetic state with in-plane spins are the preconditions. Class A: the p - d hybridization mechanism can not an in-plane polarization. Class B: double-leaf Riemann converse magnetoelectricity is possible but not guaranteed. And the dissipation of converse magnetoelectricity is unavoidable. Class C: double-leaf Riemann converse magnetoelectricity is guaranteed and dissipationless. (b) The magnitude of spin-induced polarization of some selected 2D ferromagnets in the D_{3h} category.

sipationless converse magnetoelectricity (e.g. Fig. S9 in SM [31]). In addition to these symmetry requirements, the candidate systems should be ferromagnetic and the ab -plane should be the magnetic easy plane.

Following above conditions, several materials were screened for this magnetoelectricity, including the $2H$ - MX_2 type and VSi_2N_4 monolayer. The p - d hybridization mechanism can indeed induce ferroelectric polariza-

tion in these systems, while their amplitude depends on their electronic structures especially their SOC strength, as shown in Fig. 5(b). Despite their values of polarization, all of them exhibit the double-leaf Riemann magnetoelectricity and dissipationless converse magnetoelectric function.

IV. CONCLUSION

In summary, a double-leaf Riemann surface topological magnetoelectricity has been predicted, in which the topology protects the 180° reversal of magnetization under a cycle of electric field. Based on symmetry analysis, p - d hybridization theory, and DFT calculations, the double-leaf Riemann surface topological magnetoelectricity has been demonstrated in GdI_2 monolayer and other candidates. Such a topological magnetoelectricity allows the direct and precise manipulation of magnetization by AC electric fields. Our work extends the territory of topology in condensed matter, and provides a robust solution to the long-term challenge of electrical reversal of magnetism.

ACKNOWLEDGMENTS

We thank Profs. Yunfeng Jiang and Yisheng Chai for helpful discussions on the mathematical formula of magnetoelectricity. This work was supported by the National Natural Science Foundation of China (Grant Nos. 12325401, 12274069, & 12374097) and the Big Data Computing Center of Southeast University.

-
- [1] K. Tschernig, A. Jimenez-Galan, D. N. Christodoulides, M. Ivanov, K. Busch, M. A. Bandres, and A. Perez-Leija, Topological protection versus degree of entanglement of two-photon light in photonic topological insulators, *Nat. Commun.* **12**, 1974 (2021).
 - [2] S. Tang, C. Zhang, D. Wong, Z. Pedramrazi, H.-Z. Tsai, C. Jia, B. Moritz, M. Claassen, H. Ryu, S. Kahn, J. Jiang, H. Yan, M. Hashimoto, D. Lu, R. G. Moore, C.-C. Hwang, C. Hwang, Z. Hussain, Y. Chen, M. M. Ugeda, Z. Liu, X. Xie, T. P. Devereaux, M. F. Crommie, S.-K. Mo, and Z.-X. Shen, Quantum spin hall state in monolayer $1T'$ - WTe_2 , *Nat. Phys.* **13**, 683 (2017).
 - [3] X. Kou, S.-T. Guo, Y. Fan, L. Pan, M. Lang, Y. Jiang, Q. Shao, T. Nie, K. Murata, J. Tang, Y. Wang, L. He, T.-K. Lee, W.-L. Lee, and K. L. Wang, Scale-invariant quantum anomalous hall effect in magnetic topological insulators beyond the two-dimensional limit, *Phys. Rev. Lett.* **113**, 137201 (2014).
 - [4] N. Nagaosa and Y. Tokura, Topological properties and dynamics of magnetic skyrmions, *Nat. Nanotechnol.* **8**, 899 (2013).
 - [5] A. Fert, N. Reyren, and V. Cros, Magnetic skyrmions: advances in physics and potential applications, *Nat. Rev. Mater.* **2**, 17031 (2017).
 - [6] J.-Y. Chauleau, T. Chirac, S. Fusil, V. Garcia, W. Akhtar, J. Tranchida, P. Thibaudeau, I. Gross, C. Blouzon, A. Finco, M. Bibes, B. Dkhil, D. D. Khalyavin, P. Manuel, V. Jacques, N. Jaouen, and M. Viret, Electric and antiferromagnetic chiral textures at multiferroic domain walls, *Nat. Mater.* **19**, 386 (2020).
 - [7] M. Guo, C. Guo, J. Han, S. Chen, S. He, T. Tang, Q. Li, J. Strzalka, J. Ma, D. Yi, K. Wang, B. Xu, P. Gao, H. Huang, L.-Q. Chen, S. Zhang, Y.-H. Lin, C.-W. Nan, and Y. Shen, Toroidal polar topology in strained ferroelectric polymer, *Science* **371**, 1050 (2021).
 - [8] S. Dong, J.-M. Liu, S.-W. Cheong, and Z. Ren, Multiferroic materials and magnetoelectric physics: symmetry, entanglement, excitation, and topology, *Adv. Phys.* **64**, 519 (2015).
 - [9] J. T. Heron, D. G. Schlom, and R. Ramesh, Electric field control of magnetism using BiFeO_3 -based heterostructures, *Appl. Phys. Rev.* **1**, 021303 (2014).
 - [10] F. Wang, Y. Zhou, X. Shen, S. Dong, and J. Zhang, Magnetoelectric coupling and cross control in two-dimensional ferromagnets, *Phys. Rev. Appl.* **20**, 064011 (2023).
 - [11] S. Dong, H. Xiang, and E. Dagotto, Magnetoelectricity in multiferroics: a theoretical perspective, *Natl. Sci. Rev.* **6**, 629 (2019).

- [12] J. J. Wang, J. M. Hu, J. Ma, J. Zhang, L.-Q. Chen, and C.-W. Nan, Full 180° magnetization reversal with electric fields, *Sci. Rep.* **4**, 7507 (2014).
- [13] Y. Weng, L. Lin, E. Dagotto, and S. Dong, Inversion of ferrimagnetic magnetization by ferroelectric switching via a novel magnetoelectric coupling, *Phys. Rev. Lett.* **117**, 037601 (2016).
- [14] L. F. Lin, Q. R. Xu, Y. Zhang, J. J. Zhang, Y. P. Liang, and S. Dong, Ferroelectric ferrimagnetic LiFe_2F_6 : charge ordering mediated magnetoelectricity, *Phys. Rev. Mater.* **1**, 071401(R) (2017).
- [15] J. Chen and S. Dong, Manipulation of magnetic domain wall by ferroelectric switching: Dynamic magnetoelectricity at the nanoscale, *Phys. Rev. Lett.* **126**, 117603 (2021).
- [16] L. Ponet, S. Artyukhin, Th.Kain, J. Wettstein, A. Pimenov, A. Shuvaev, X. Wang, S.-W. Cheong, M. Mostovoy, and A. Pimenov, Topologically protected magnetoelectric switching in a multiferroic, *Nature* **607**, 81 (2022).
- [17] G. Liu, M. Pi, L. Zhou, Z. Liu, X. Shen, X. Ye, S. Qin, X. Mi, X. Chen, L. Zhao, B. Zhou, J. Guo, X. Yu, Y. Chai, H. Weng, and Y. Long, Physical realization of topological roman surface by spin-induced ferroelectric polarization in cubic lattice, *Nat. Commun.* **13**, 2373 (2022).
- [18] Z. Wang, Y. Chai, and S. Dong, First-principles demonstration of roman surface topological multiferroicity, *Phys. Rev. B* **108**, L060407 (2023).
- [19] J. E. Mee and J. D. Corbett, Rare earth metal-metal halide systems. VII. the phases gadolinium 1.6-chloride and gadolinium diiodide, *Inorg. Chem.* **4**, 88 (1964).
- [20] G. Kresse and J. Furthmüller, Efficient iterative schemes for ab initio total-energy calculations using a plane-wave basis set, *Phys. Rev. B* **54**, 11169 (1996).
- [21] G. Kresse and J. Furthmüller, Efficiency of ab-initio total energy calculations for metals and semiconductors using a plane-wave basis set, *Comp. Mater. Sci.* **6**, 15 (1996).
- [22] P. E. Blöchl, Projector augmented-wave method, *Phys. Rev. B* **50**, 17953 (1994).
- [23] G. Kresse and D. P. Joubert, From ultrasoft pseudopotentials to the projector augmented-wave method, *Phys. Rev. B* **59**, 1758 (1999).
- [24] Y. Wang and J. P. Perdew, Correlation hole of the spin-polarized electron gas, with exact small-wave-vector and high-density scaling, *Phys. Rev. B* **44**, 13298 (1991).
- [25] S. L. Dudarev, G. A. Botton, S. Y. Savrasov, C. J. Humphreys, and A. P. Sutton, Electron-energy-loss spectra and the structural stability of nickel oxide: An LSDA+U study, *Phys. Rev. B* **57**, 1505 (1998).
- [26] B. Wang, X. Zhang, Y. Zhang, S. Yuan, Y. Guo, S. Dong, and J. Wang, Prediction of a two-dimensional high- T_C f-electron ferromagnetic semiconductor, *Mater. Horizons* **7**, 1623 (2020).
- [27] A. V. Krūkau, O. A. Vydrov, A. F. Izmaylov, and G. E. Scuseria, Influence of the exchange screening parameter on the performance of screened hybrid functionals, *J. Chem. Phys.* **125**, 224106 (2006).
- [28] A. Togo and I. Tanaka, First principles phonon calculations in materials science, *Scripta Mater.* **108**, 1 (2015).
- [29] R. D. King-Smith and D. Vanderbilt, Theory of polarization of crystalline solids, *Phys. Rev. B* **47**, 1651 (1993).
- [30] D. Xiao, G.-B. Liu, W. Feng, X. Xu, and W. Yao, Coupled spin and valley physics in monolayers of MoS_2 and other Group-VI dichalcogenides, *Phys. Rev. Lett.* **108**, 196802 (2012).
- [31] See Supplimental Material for electronic structure, magnetic ground state, magnetic symmetry analysis, more results of micromagnetic simulations of GdI_2 monolayer, and derivation of the magnetoelectric tensors for 2D point groups, including Ref. [37].
- [32] A. Kasten, P. H. J. Mueller, and M. Schienle, Magnetic ordering in GdI_2 , *Solid State Commun.* **51**, 919 (1984).
- [33] H. Murakawa, Y. Onose, S. Miyahara, N. Furukawa, and Y. Tokura, Ferroelectricity induced by spin-dependent metal-ligand hybridization in $\text{Ba}_2\text{CoGe}_2\text{O}_7$, *Phys. Rev. Lett.* **105**, 137202 (2010).
- [34] J. Zhang, Y. Zhou, F. Wang, X. Shen, J. Wang, and X. Lu, Coexistence and coupling of spin-induced ferroelectricity and ferromagnetism in perovskites, *Phys. Rev. Lett.* **129**, 117603 (2022).
- [35] T.-H. Arima, Ferroelectricity induced by proper-screw type magnetic order, *J. Phys. Soc. Jpn.* **76**, 073702 (2007).
- [36] C. Jia, S. Onoda, N. Nagaosa, and J. H. Han, Bond electronic polarization induced by spin, *Phys. Rev. B* **74**, 224444 (2006).
- [37] M. Matsumoto, K. Chimata, and M. Koga, Symmetry analysis of spin-dependent electric dipole and its application to magnetoelectric effects, *J. Phys. Soc. Jpn.* **86**, 034704 (2017).